Coatings for Fibre and Interphase Modification in a Cementitious Matrix

Obwohl Glasfasern bereits seit Jahrzehnten als Verstärkung von Zementmatrizes in Betracht gezogen werden, sind die strukturellen Anwendungen durch ihre geringe Korrosionsresistenz gegenüber stark alkalischer Umgebung begrenzt. Es wird ein preisgünstig anwendbares Verfahren beschrieben, bei dem eine nanoskalige polymere Oberflächenbeschichtung auf Basis von Styren-Butadien-Copolymeren in verschiedenen Konzentrationen auf alkaliresistente Glasfasern (ARG) appliziert wird. Die Zug- und Grenzflächeneigenschaften von Glasfasern und Composites werden durch Einzelfaserzugversuche, Einzelfaser- sowie Rovingauszugversuche und Längszugtests charakterisiert. Die Veränderungen der Oberflächeneigenschaften der Fasern werden bewertet am Beispiel der Oberflächensteifigkeiten und der lokalen Adhäsionskräfte unter Anwendung der Rasterkraftmikroskopie (AFM) mit der Nanoindentation-Technik. Die Ergebnisse zeigen, dass die polymere Beschichtung der Glasfasern sowohl zu einer signifikant verbesserten Korrosionsbeständigkeit gegenüber Alkalien als auch einer erhöhten Bruchenergie der Composites führt.

Keywords
alkaline resistant glass fibre
cement matrix
coating
sizing
adhesion strength
fracture energy
atomic force microscopy
pull-out test
nanoindentation technique
corrosion resistance

Bearbeiter
S.-L. Gao
E. Mäder
R. Plonka

Förderer
Deutsche Forschungsgemeinschaft, Sonderforschungsbereich 528

Kooperation
Technische Universität Dresden, Fakultät Bauingenieurwesen, Institut für Tragwerke und Baustoffe, Fakultät Maschinenwesen, Institut für Textil- und Bekleidungstechnik

Gastwissenschaftler
Dr. S. Zhandarov, Metall-Polymer-Forschungsinstitut der Akademie der Wissenschaften Weissrusslands, Gomel

1 Introduction

The sizings on the glass fibre surface are responsible to enable the manufacture and performance of the fibres, particularly the surface protection, abrasion resistance, strength maintenance, and interphase formation of composites produced [1, 2]. The alkali-resistant glass fibre (ARG) was preferably designed to reinforce cementitious matrices which have been widely used in construction and civil engineering with a great deal of success since the late 1960's [3]. It has been reported, however, that the tensile strength and the impact strength of ARG fibre-reinforced cement products decrease due to possible corrosive reactions between the fibre surface and the matrix during aging [4, 5].
For improving the long-term performance of glass/fibre-reinforced cement, it is thus very important to develop new types of coatings to modify the ARG fibre surface and improve their durability. Furthermore, it is important to examine, for the improvement of the composite performance, how the coatings interact with the surrounding cementitious matrix. The thin sizing on commercial ARG, which is typically a few tens of nanometer in average thickness, basically consists of components of a organo-silane coupling agent, a polymer film former and a lubricant, leading to variable properties and great difficulty in both process control and *in-situ* characterization. Therefore, little has been solidly established about the mechanical properties, morphology, and exact corrosion mechanisms of the polymer coatings and/or fibre surface layer in various environmental conditions. In order to gain insight into what mechanisms are responsible for variation of fibre tensile strength and interphase property after exposure to concentrated alkaline environmental attacks, investigation of the surface and interphase morphology, chemical composition and both macro- and nanoscopic mechanical behaviours was conducted.

2 Experimental

2.1 Fibres and Surface Treatments

The fibre samples used in this work were NEG ARG 620-01 fibres, with an average diameter of 13 µm and organic sizing content of 0.6 wt-%, supplied by Nippon Electric Glass Co. Ltd. We applied additional surface coatings based on styrene-butadiene with varied concentrations, since styrene-butadiene dispersions had previously been found to be the most resistant in alkaline solutions [6]. The additionally coated fibres, namely C1 and C2, have coating contents of about 2.4 and 7 wt-%, respectively.
To predict the long-term behaviour of ARG fibres in concrete in a short term, recently, we have employed accelerated aging methods that entail raising alkalinity and temperature of the test environment aging [7]. Here, we only extracted the above three kinds of fibres in a selected highly concentrated alkaline aqueous solution (5 wt-% NaOH at 23 °C for 28 d, pH = 13), which is the most aggressive and corrosive condition to the fibre surface out of the tested ones under ambient temperature.

2.2 Composites

The interaction of fibre surface with cement was investigated by the roving pull-out test, where the rovings were embedded in cementitious matrix (CEM I 52.5) at a constant embedding length of 10 mm. Thus, for a first approximation the maximum force of each force-displacement curve was determined. In addition, rectangular composite specimens were made for tensile tests with three continuous fibre bundles embedded in the cementitious matrix along the centre line. The composites were cured at ambient temperature in wet environments (100 % relative humidity, RH) for 28 d.

2.3 Fibres Strength

The single fibre tensile test was conducted under 65 % RH and 20 °C using the Fafegraph ME testing device (Fa. Textechno) equipped with a 10 N force cell. The test cross velocity is 0.5 $mm \cdot min^{-1}$ and the gauge length is 20 mm in accordance with EN ISO 5079. Based on a vibration approach, the fineness of each selected fibre was determined by a Vibromat ME (Fa. Textechno) in accordance with EN ISO 53812 and ASTM D 1577.

2.4 Surface Properties

A scanning force microscope (a Digital Instruments D3100, USA) was used as both a surface imaging tool and a nano-indentation device to evaluate the fibre and surface properties. The topography of samples was studied in tapping mode. The cantilever (ULTRASHARP NSC16/50, MikroMasch, Estonia) has a normal spring constant of 35 $N \cdot m^{-1}$, a tip cone angle of 20°, radius of 5 to 10 nm and modulus of 160 GPa to assure good imaging resolution and nanometer scale indents.
FTIR-ATR spectroscopic measurements were performed to monitor the chemical changes in the fibre surface layer using a Bruker spectrometer IFS 66v with a Golden Gate Diamant ATR unit (Ge crystal, penetration depth 166-1106 nm at 4000-600 cm^{-1}). In addition, pyrolysis (60 min, 600 °C) was used to detect the surface coating's content.
Electrokinetic investigation by an Electrokinetic analyser EKA (A. Paar, Austria) allows to estimate both type and amount of disso

ciable surface functional groups on the fibre surfaces and to predict adsorption processes influenced by interaction forces at the surface.
For quasi-static single fibre pull-out tests specimens were made by means of the technique described previously [6] and optimized testing conditions.

2.5 Composite Interphase Properties

The roving pull-out and mechanical tensile tests of composite specimen were performed on an universal testing machine with a constant crosshead speed of 1 mm·min^{-1}. The fracture surface was examined using a scanning electron microscope (LEO 435VP).

3 Results and Discussion

3.1 Fibre mechanical properties and surface topography

We first investigated the tensile performance of the single fibres, together with its surface properties. A summary of the mechanical properties and surface roughness data is presented in Fig. 1. In agreement with our previous report [7], the commercially available alkali-resistant glass fibre shows extensive strength loss after alkali attack. Here we observed that coated glass fibres have a remarkably higher tensile strength (30 %) than the control NEG fibres after long-term conditioned in a highly alkaline environment, demonstrating our organic materials that are applied on the glass fibre surface resulting in a significantly improved corrosion resistance to alkali. On the other hand, the coating introduced high surface roughness values in terms of R_a, R_{max} and standard deviation (Fig. 1b) indicates that the inhomogeneous surface coating resulted stress concentration might also be partly responsible for the reduction in the tensile strength of the coated fibres. Consequently, the coated fibres before and after extraction show roughly similar average strength values regardless of the coating concentrations.

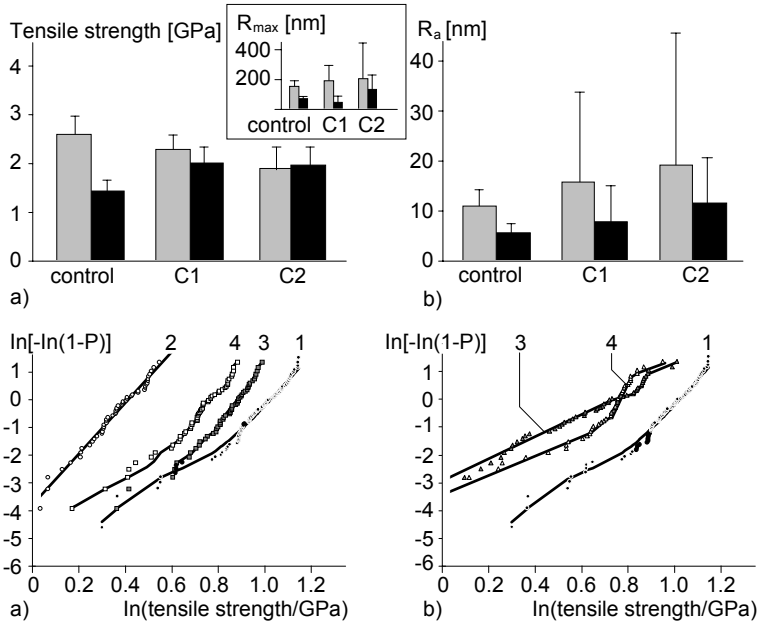

Fig. 1:
Effect of the surface coating of NEG fibres on (a) the average tensile strength (at a gauge length of 20 mm) and (b) image mean roughness, R_a, maximum height roughness, R_{max} (insert picture) with standard deviation before (▭) and after extraction in 5 wt-% NaOH aqueous solution with a pH = 13 (■) at ambient temperature for 28 d. Data are mean ± S.D. from 50 and 10 separate tensile and AFM tests, respectively.

Fig. 2:
Comparison of Weibull plots of fracture probability as a function of tensile strength for NEG and C1 (a) and C2 (b) fibres before (3) and after extraction in 5 wt-% NaOH aqueous solution with a pH of 13 (4) at ambient temperature for 28 days, control (1), and control after extraction in 5 wt-% NaOH aqueous solution with a pH of 13 (2)

To verify the effect of surface properties on the statistical distribution of fibre tensile strength, the classification of fracture can be based on two modes: i) intrinsic failure characterized by fibre

internal defects and surface defects which are not influenced by either the sizing or surface treatments; (ii) extrinsic failure characterized by surface flaws which are strongly surface property dependent. The cumulative probabilities of failure for single and bimodal Weibull distribution function are given by following analytical formulae [7, 8], respectively:

Single modal:

$$P = 1\text{-}\exp\left[-\left[\frac{\sigma}{s_0}\right]^{m_0}\right] \tag{1}$$

Bimodal:

$$P = 1\text{-}\exp\left[-\kappa(d)\cdot\left[\frac{\sigma}{s_e}\right]^{m_e}\right] + f_i\left\{\exp\left[-\kappa(d)\cdot\left[\frac{\sigma}{s_e}\right]^{m_e}\right] - \exp\left[-\left[\frac{\sigma}{s_i}\right]^{m_i}\right]\right\} \tag{2}$$

where P is the cumulative probability of failure [i/(n+1)] at the tensile stress σ. The parameters m_0 and s_0 are the Weibull shape factor (or modulus, slope of the distribution) and the scale factor (or characteristic strength) of fractured fibres, respectively. The fraction of intrinsic failure is f_i and $\kappa(d)$ is a coefficient dependent on the effective surface thickness. Fig. 2 shows a detailed description of the experimental data by either single two-parameter Weibull cumulative distribution function (CDF) or bimodal Weibull CDF. From the single Weibull best-fit lines, only the control NEG after NaOH surface treatments result to apparent lower scale but higher shape parameters than that of the others, indicating more severe flaws but a lower heterogeneity. It suggests that the treatments provide additional surface flaws with similar severity and, thus, flaw homogeneity relative to the control and coated fibres. As expected, the bimodal curves are in general more suitable for the description of the nonlinear probability plots than the single Weibull lines. Since the irregular sizing distribution on the control and coated fibres could lead to both surface flaw being partly healed and local stress concentration, resulting in different flaw severities and the plots show different slopes. For the C2 fibres with the highest average coating thickness of 266 nm, the alkaline extraction reduced its surface roughness (Fig. 1b), the surface stress concentration effect could be partly removed. The C1 and C2 fibres after extraction, therefore, exhibited a very similar average tensile strength values.

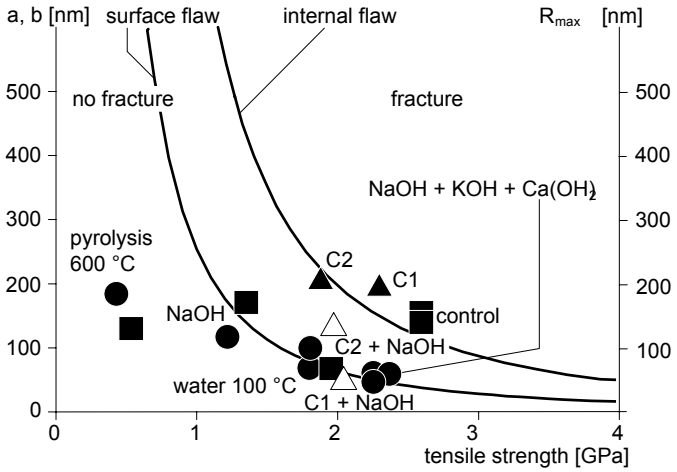

Fig. 3:
Comparison of the measured maximum height surface roughness (R_{max}) with the Griffith strength prediction for NEG (■), VET (●) and NEG + styrene-butadiene fibres (▲) before and after (△) various surface treatments. Of interest is the tensile strength of the coated fibres remains approximately unchanged after NaOH treatment.
a, b = maximum surface and internal defect size, respectively.

We can go further by considering the correlation (Fig. 3) of surface roughness and Griffith fracture criterion to provide a better understanding of the mechanisms and controlling factors affecting the

performance and durability of ARG fibres. Here we treat the fractures as the result of a competition between external surface and internal flaws as a simple interpretation of the above complicated statistical phenomenon. The former case can be modelled as externally circumferentially cracked rod in tension where the crack length a is assumed to be far smaller than the diameter of the rod; the later one can be simulated as a penny-shaped flaw (length of 2b) in an infinite body under tension [9]. According to our results of AFM characterization, one interesting observation is that the maximum height roughness followed very closely the line predicted by the Griffith fracture criterion, except for the cases of the control, coated C1 and C2 (C2+NaOH), and pyrolyzed fibres.
In the case of the pyrolysis, the fracture is dominated by the probably enlarged internal flaws from the high temperature, which is consistent with the above observation of the unimodal failure distribution [7]. Indeed, the higher the maximum height roughness the bigger the most severe flaw will be present in the surface layer and, consequently, the lower the expected value of the ultimate tensile strength.

3.2 Fibre surface mechanical and chemical properties

We then in-situ examined the fibre surface elastic/adhesion properties together with surface chemical characteristics. Our nano-indentation tests at a range of indentation forces were made, as shown in Fig. 4, to provide an indication of the variability of the local contact stiffness/adhesion properties. It can be observed that the control and coated fibres show very different behaviour of stiffness curve shift after alkali attack. Specifically, the stiffness values significantly decrease for the control NEG. This was unexpected, as the apparent contact stiffness should increase when the substrate glass dominates the elastic deformation because of the reduced thickness or totally disappear of the organic sizing layer by the alkalinity. Thus, we conclude that the chemical corrosion causes a reduction of the intrinsic glass surface properties. This is also supported by the aforementioned tensile strength and previous imaging observation of the microrough porous surface without sizing [7].

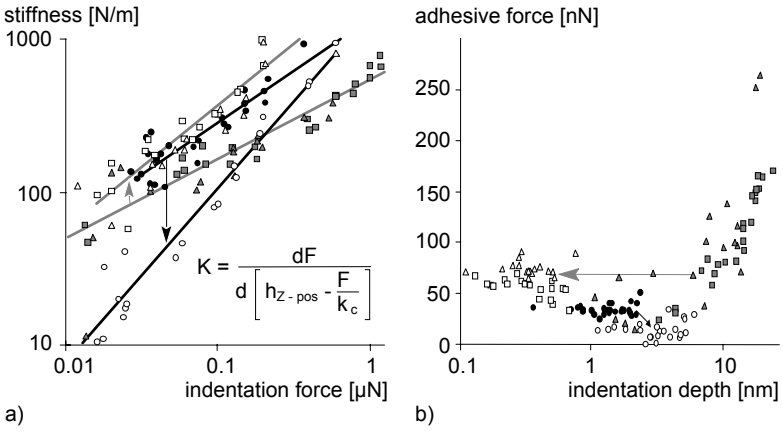

Fig. 4:
AFM determination of (a) contact stiffness vs. indentation force and (b) adhesive forces vs. indentation depth for the silicon tip on the surfaces of NEG fibres. The contact stiffness, K, is the slope dF/dh of the initial elastic unloading curve which includes contributions from both the specimen and the indenter. Variation of the nano-scale surface properties subjected to alkali attack are indicated by the arrows. Control (●), C1 (■), C2 (▲), control + NaOH (○), C1 + NaOH (□), C2 + NaOH (△)

In sharp contrast, the stiffness value of the styrene-butadiene coated fibres after extraction is slightly higher than the control and original coated specimen. This is clearly attributed to the sizing layer being partly removed (Fig. 1b) but the intrinsic glass surface properties might being free of corrosion, which is further confirmed by the FTIR-ATR results.
Similarly, the surface adhesion force allows us to check alkali resistance ability of coating (Fig. 4b). It is believed that the total inter

action between the tip and sample surface is the sum of several individual forces, like van der Waals, ionic bonding between the functional groups, electrostatic double layer forces, and hydration forces. Remarkably, compared to the control specimen, the magnitude of the adhesive force of alkali treated NEG is much reduced. The styrene-butadiene coated fibres show a strong function of the indentation depth, in other words, interaction surface area arising from the relatively thick polymer coating layer (101 nm and 266 nm for C1 and C2, respectively). Importantly, their magnitudes range of the adhesive forces are not greatly influenced by the alkali extraction, which provided additional evidence of the intrinsic surface properties might being free of corrosion.

We confirmed the above trends directly through the use of zeta-potential and FTIR-ATR investigations. Electrokinetic measurements reveal the zeta-potential due to acidic and/or basic groups at a surface layer and allow to predict their interaction with the environment. The control commercial NEG fibre possesses a negative zeta-potential and an isoelectric point (IEP) of about pH 5. This surface is dominated by acidic groups. Due to the styrene-butadiene coating (C2) the plateau value and IEP is shifted to more negative values. This is aimed to buffer the alkaline groups of the cementitious matrix and thus avoid damage of the glass fibre itself. By testing both commercial and our coated fibres after alkali extraction a lifetime estimation is aimed. For the control fibre the IEP shifted to a higher pH value and the plateau region disappeared.

This behaviour was identified earlier for acidic surface layers on E-glass fibres [10] and is in agreement with rest sizings left on the surface interacting with increasing anions concentrations. Interestingly, the acidic groups on the coated fibre's surface still dominate after NaOH treatment indicated by the plateau value and low IEP. The shift to more negative zeta-potential might be due to topological effects.

In addition, no hints for sizing on the control specimen after alkali extraction could be found in the ATR-Spectra [21]. It is generally known that the ν(C=O) stretch of functional group typically lies around 1720 cm^{-1} while the 1510 cm^{-1} peak is assigned to the *para* substituted benzene rings found in the commercially available sizing film former backbone [11]. The absorption peaks in the range 3050-2850 cm^{-1} correspond to the C–H bonds. Very broad bands in the carboxylate region at ~1567 cm^{-1} are probably due to a variety of carbonate species on zirconia. Since on the original fibre a sizing was detected, a difference spectra was determined. This difference spectra is equal to the summary of the previously determined spectra of the ethanol and hexane extraction. The spectra before and after alkali treatment for coated fibres are hardly different. The difference spectra only reveal two shoulders at 1550 and 1445 that indicate a possible salt formation (carboxylates). Overall, the surface chemical structure information is strongly consistent with the macro and micro mechanical characterization. Our data indicated that the coating developed in this study is chemically inert to the alkali environment.

3.3 Determination of adhesion strength and energy release rate

Three techniques aimed at determining interfacial parameters (τ_f and τ_d, G_{ic}, τ_{max2}, n, etc., in accordance with the particular model) were used for experimental data treatment:

1. Calculating τ_d and G_{ic} from the *kink* force, F_d, for each individual

force-displacement curve. For stress-based analysis (τ_d), we used the eq. (3).

$$\tau_d = \frac{F_d \beta}{\pi d_f} \coth(\beta l_e) + \tau_T \tanh\frac{\beta l_e}{2}, \quad (3)$$

where β is the shear-lag parameter as determined by Nayfeh [12], l_e is the embedded fibre length, and τ_T is a stress term due to thermal shrinkage [13], which can be neglected for cement matrices. For energy-based analysis, G_{ic} values were calculated from a similar equation derived by Nairn [14]. After this, we determined τ_f using the obtained τ_d or G_{ic} value and the peak load, F_{max}, recorded for this specimen. (In fact, this second procedure is the force-displacement curve modeling using these τ_d (G_{ic}) and F_{max} values.)

2. The eq. (4) gives the current load, F, applied to the fibre, as a function of the crack length, a, for a specimen with a given embedded length, l_e. Generating many F(a) curves for different embedded lengths (e.g., for the range $0 < l_e \leq 1.5$ mm, with a 5 μm increment in l_e) and plotting their maximum values versus l_e, we obtain F_{max} as a function of the embedded length in the stress-based model [13, 15, 16].

$$F = f_s = \frac{\pi d_f}{\beta}\left\{\tau_d \tanh\left[\beta(l_e - a)\right] - \tau_T \tanh\left[\beta(l_e - a)\right] \cdot \tanh\left[0.5\,\beta(l_e - a)\right] + \beta\tau_f a\right\} \quad (4)$$

This function includes τ_d and τ_f as fitting parameters; using a standard least-squares method, it is possible to obtain the best fit, i.e., a pair of (τ_d, τ_f) values which minimizes the sum

$$S = \sum_i \left[F_{max}^{exper}(\tau_d, \tau_f, \ldots) - F_{max}^{theor}(\tau_d, \tau_f, \ldots)\right]^2 \quad (5)$$

This procedure was described in detail in [13] and extended to the energy-based model of debonding (best fit for G_{ic} and τ_f) in [16]. In this investigation, the fitting algorithm was modified in order to take into account the scatter in individual fibre diameters.

3. Improved model with two-stage debonding, originally proposed by Brameshuber et al. [17, 18]. Carrying out a five-parameter least-squares analysis, as was suggested in original papers, is rather time-consuming and may yield ambiguous results. For instance, two different sets of their model parameters can produce very similar force-displacement curves, since, e.g., the variation in τ_2 can be compensated by a suitable variation in n. We modified the original model, first of all, by equating their shear-lag parameter, λ_l, to the Nayfeh's parameter, β; then, the free fibre length was determined from the slope of the initial (elastic) part of the force-displacement curve and used in further analysis (s_{cr} can be calculated using the known β value); the τ_d value was calculated from the *kink* force, and τ_f, from the region corresponding to post-debonding friction; and finally τ_2 and n were determined using a least-squares method (by fitting the experimental pull-out curve) with only these two fitting parameters. Here we should note that τ_d in this model has different physical meaning than τ_d in traditional stress-based models of debonding, since it corresponds to the beginning of the second stage of debonding ("bond softening") rather than full debonding.

Tab. 1 presents the τ_d and τ_f values for glass fibre-cement matrix systems calculated within the frames of the stress-based model using individual force-displacement curves (with F_d and F_{max} as key experimental data) and using a two-parameter least squares method to fit experimentally obtained $F_{max}(l_e)$ relationships by theoretical functions. In Tab. 2, energy-based interfacial parameters for these systems (G_{ic} and τ_f) are presented and compared.

Table 1:
Local interfacial shear strength (τ_d) and interfacial frictional stress (τ_f) in NEG fibres- cement matrix systems estimated using individual force-displacement curves (1) and two-parameter fit of the maximum force as a function of embedded length (2)

Fibres		NEG ARG 620-01		NEG ARG 620-01/2		NEG ARG 620-01/2b	
		τ_d [MPa]	τ_f [MPa]	τ_d [MPa]	τ_f [MPa]	τ_d [MPa]	τ_f [MPa]
Untreated	1	23.3± 8.0	4.6 ± 1.9	34.1±11.0	3.3 ± 1.7	25.1±11.2	1.3 ± 1.0
	2	60.8	2.4	91.8	0.2	–	–
NaOH treated	1	28.1± 6.4	1.7 ± 0.4	39.6±11.7	5.1 ± 2.5	38.9±10.8	3.2 ± 1.5

Table 2:
Critical energy release rate (G_{ic}) and interfacial frictional stress (τ_f) in NEG fibres – cement matrix systems estimated using individual force-displacement curves (1) and two-parameter fit of the maximum force as a function of embedded length (2)

Fibres		NEG ARG 620-01		NEG ARG 620-01/2		NEG ARG 620-01/2b	
		G_{ic} [J/m^2]	τ_f [MPa]	G_{ic} [J/m^2]	τ_f [MPa]	G_{ic} [J/m^2]	τ_f [MPa]
Untreated	1	0.6 ±0.07	4.6 ± 1.9	1.29±0.1	3.3 ± 1.7	0.7 ± 0.1	1.3 ± 1.0
	2	4.0	2.6	10.4	0.4	–	–
NaOH treated	1	0.87±0.06	1.7 ± 0.4	1.74±0.1	5.1 ± 2.5	1.68 ± 0.1	3.2 ± 1.5
	2	1.8	0.83	8.3	0.78	–	–

First of all, the local interfacial shear strength (τ_d) values calculated from the *kink* force seem to be quite plausible. For glass fibres combined with cement matrices, the local interfacial shear strength is somewhat smaller compared with polymer matrix composites, which indicates weaker physicochemical bonding between the fibre surface and the matrix and can be due, in part, to the presence of voids near the interface. The τ_f values determined using this method for all systems are in good agreement (within 20 % error) with the frictional stress estimated from the post-debonding regions of the force-displacement curves, which further evidences the accuracy of the technique used.

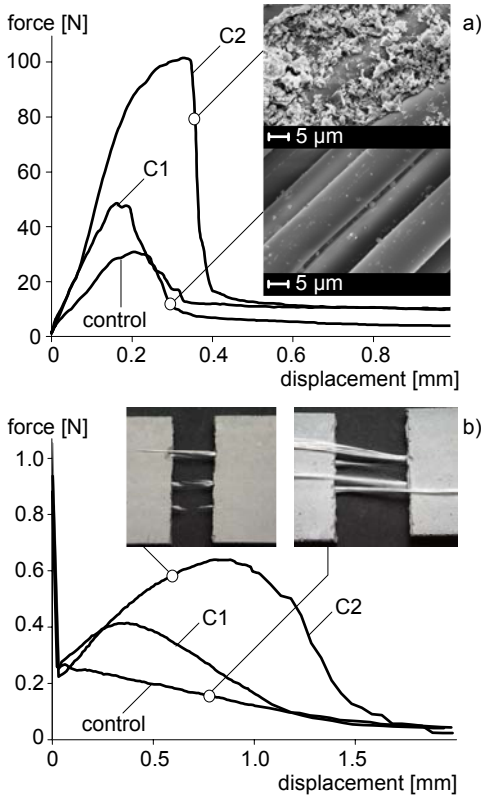

Fig. 5:
Average force-displacement curves of (a) roving pull-out tests and (b) composite tensile tests with control NEG and coated C1 and C2 fibres. The insert pictures show the fracture structures of the specimens.

Since the derivation of the critical energy release rate, G_{ic}, from F_d values is based on the same principles and assumption on which

the τ_d calculation is based (cf. [15, 19]) and G_{ic} and τ_d are related by a (polynomial) function [15, 16], G_{ic} values in Tab. 2, calculated from individual force-displacement curves, can also be regarded as reliable. The critical energy release rate was much less than for glass fibre-polymer composites, which can be attributed to both very low level of interfacial adhesion and less deformability than for the polymer matrix. As for frictional stress values, these are practically identical to those obtained using the stress-based approach.
Theoretical simulation of force-displacement curves using the model by Brameshuber et al. [17, 18] yielded τ_d and τ_f values very similar to those obtained by traditional linear elastic models. However, this model gives additional information on the imperfect interface at the second stage of debonding. It allows estimation of *inelastic* parameters (τ_{max2} and n) which help to characterize the *degree of perfection* (τ_{max2}/τ_d) and the deformability at the second stage of debonding. For the investigated cement-glass systems the typical values were τ_{max2}/τ_d = 0.9 and n = 1.4, which shows that inelastic effects in these systems were distinct but not prevailing. For pull-out test with polymer matrices, a similar model but using different bond law was developed [20], which can be used to predict force-displacement curves and to determine interfacial parameters for two-stage debonding with interface yielding.

3.4 Composite and interphase fracture performance

We examined the effect of polymer coating on the fibre bundles reinforced actual concrete composites activated by roving pull-out and longitudinal tensile fractures. It can be clearly seen (Fig. 5) that the coated fibre bundles with higher coating content (C2) show a significantly higher maximum fracture force, post-debonding friction force and the fracture energy.
Proposed explanations for this behaviour are integrating of the fibres by coating bridging (particularly for the C2) and the consequent increase in the frictional component of bond or a much less degradation due to limited access of the aggressive solution to the inner part of the fibre bundles. We noted that, from high magnification SEM analysis (Fig. 5a) of the interfacial region, a portion of the cement matrix that was bonded on the fibres after pull-out, which indicated that the coating causes not only improved corrosion resistance of glass fibre itself but also strong interfacial bonding and associated fracture toughness of its composites. For concrete composite containing glass fibres whose maximum strain is greater than that of the cement, the crack propagating in the matrix is halted by the stiff fibre. With further increase in the external load, the interfacial debonding will extend some distance along the fibre bundle. Then the successive fracture of all the fibres is the dominated behaviour. Consequently, pull-out and friction is the final process. The total energy absorption mechanisms during the composite fracture process should mainly contribute from the coexistence work of deformation and generation of new surfaces, successive fracture of all the fibres (Fig. 5b), interfacial debonding and friction associated with fibre pull-out, as well as stress redistribution. A detailed explanation of the failure mechanisms using our new model associated with localized interphase bundle, resulting in quite long pull-out lengths of the fibres (Fig. 5b). Overall, although the hydration concrete products are highly corrosive alkali, our polymer coating not only provides good protection from the corrosion attack for the glass fibre itself but also improved energy absorption capability of its composites.

4 Conclusion

An improved durability of the alkali-resistant glass fibres is achieved by nano-coatings based on styrene butadiene polymer dispersions. An assessment of changes in the fibre surface chemical and nanomechanical properties is provided for understanding the fibre bulk mechanical fracture behaviour. The effect of tensile strength and nano-roughness variability on the statistical analysis is correlated with Griffith fracture predictions. Sizings and coatings on ARG are found to significantly influence the tensile strength of alkali-resistant filament yarns, the adhesion strength with cementitious matrices and fracture energy of the composites. Our study indicates that the chemistry of the interaction between both sizing and coating with the cementitious matrix, the concentration of the coating, and the mechanical properties of the coatings are essential for improving the composite strength and failure energy absorption capability.

Further development of homogeneous nanocoatings with improved adhesional and mechanical properties is necessary. The chemistry of the glass fibre sizings and their conditions of interaction (dry or wet state) allows variation of adhesion strength and modified interphases. A roving pull-out test allows a rough estimation of the failure behaviour for differently sized and coated reinforcement yarns and their interaction with cementitious matrices. Microscopic investigation of the pulled-out rovings, the failed single fibres in the fill-in zone, and the failure mode is expected to contribute to the explanation of the reinforcement mechanisms.

References

[1] Mäder, E.; Mai, K.; Pisanova, E.: Compos. Interfaces 7 (2000), pp. 133-147.
[2] Zinck, P.; Mäder, E.; Gerard, J.F.: J. Mater. Sci. 36 (2001), pp. 5245-5252.
[3] Majumdar, A.J.; Ryder, J.F.: Glass Technol. 9 (1968), pp. 78-84.
[4] Majumdar, A.J.; Nurse, R.W. Mater. Sci. Engin. 15 (1974), pp. 107-127.
[5] Al-Dulaijan, S.U.: Ph.D. Thesis, The Pennsylvania State University, 1996.
[6] Mäder, E.; Plonka, R.; Schiekel, M.; Hempel, R.: Proceedings of the Techtextile Symposium 2003, (Frankfurt, Germany), pp. 4.12 and 1-10.
[7] Gao, S.L.; Mäder, E.; Abdkader, A.; Offermann, P.: Langmuir 19 (2003), pp. 2496-2506.
[8] Weibull, W.: J. Appl. Mech. 18 (1951), pp. 293-297.
[9] Gao, S.L.; Mäder, E.; Abdkader, A.; Offermann, P.: J. Non-Cryst. Solids 325 (2003), pp. 230-241.
[10] Mäder, E.; Jacobasch, H.J.; Grundke, K.; Gietzelt, T.: *in:* "Prog. Adv. Mat. Mechan." / Editor: Wang Tzuchiang; Tsu-Wei Chou. – Peking (China) : Peking University Press, 1996, pp. 905-910.
[11] Gorowara, R.L.; Kosik, W.E.; McKnight, S.H.; McCullough, R.L.: Composites A32 (2001), pp. 323-329.
[12] Nayfeh, A.H.: Fibre Sci. Technol. 10 (1977), pp. 195–209.
[13] Zhandarov, S.F.; Mäder, E.; Yurkevich, O.R.: J. Adhesion Sci. Technol. 16 (2002), pp. 1171-1200.
[14] Nairn, J.A.: Adv. Composites Lett. 9 (2000), pp. 373–383.
[15] Zhandarov, S.F.; Pisanova, E.; Mäder, E.: Composite Interfaces 7 (2000), pp. 149-175.
[16] Zhandarov; S.F.; Mäder, E.: J. Adhesion Sci. Technol. 17 (2003), pp. 967-80.
[17] Brameshuber, W.; Banholzer, B.: Beton- und Stahlbetonbau 96 (2001), pp. 663-669.
[18] Brameshuber, W.; Banholzer, B.; Brümmer, G.: Beton- und Stahlbetonbau 95 (2000), pp. 702–706.
[19] Scheer, R.J.; Nairn, J.A.: J. Adhesion 53 (1995), pp. 45-48.
[20] Zhandarov; S.; Mäder, E.: Determination of interfacial parameters in fibre-polymer systems from a pull-out test data using a bilinear bond law. – Composite Interfaces, in press.
[21] Gao, S.L., Mäder, E., Plonka, R.: Coatings for glass fibres in a cementitious matrix. – Acta Materialia, in press.